Icarus 222 (2013) 122–136

Contents lists available at SciVerse ScienceDirect

Icarus

journal homepage: www.elsevier.com/locate/icarus

Persistently illuminated regions at the lunar poles: Ideal sites for future exploration

Emerson J. Speyerer *, Mark S. Robinson

School of Earth and Space Exploration, Arizona State University, PO Box 873603, Tempe, AZ 85287-3603, United States

ARTICLE INFO

Article history:
Received 6 November 2011
Revised 16 October 2012
Accepted 19 October 2012
Available online 27 October 2012

Keywords:
Moon
Moon, Surface
Image processing

ABSTRACT

The Lunar Reconnaissance Orbiter Camera (LROC) provides multi-temporal and high resolution imaging of the north and south polar regions. These images delimit illuminated areas from those in shadow, and are used to analyze the illumination environment of the polar regions over the course of a lunar year. The Wide Angle Camera (WAC) provides repeat imaging of the north and south pole at a frequency of roughly 2 h with a ground sampling distance of 100 m. The LROC Narrow Angle Camera (NAC) acquires images with a ground sampling distance of 0.5–2.0 m providing the means to construct high resolution maps that reveal illuminated terrain under varying lighting conditions. With the multi-temporal coverage provided by the WAC and the high resolution images from the NAC, the LROC dataset enables a more comprehensive analysis of the illumination conditions near the lunar poles than any previous image based dataset. Furthermore, these images are used to validate previously published numerical models that simulate polar illumination conditions. From our analysis of the LROC images, we identified localized regions where the lunar surface remains illuminated for nearly 94% of the year with the longest eclipsed period lasting only 43 h. We also identified small illuminated peaks (tens of meters across) in areas previously modeled to be in shadow. Together, the WAC and NAC dataset provide direct, high resolution observations of the actual surface illumination environment of potential exploration sites near the lunar poles.

1. Introduction

The spin axis of the Moon is tilted by 1.5° with respect to the ecliptic normal (compared with the Earth's 23.3° ± 1.3° tilt), leaving many crater interiors and local depressions near the poles in permanent shadow, while select crater rims and local massifs remain sunlit for an extended portion of the year (Urey, 1952; Mutch, 1970; Ward, 1975; Burke, 1985; Laskar et al., 1993; Siegler et al., 2011). Both regions provide unique environments for future human and robotic explorers. Theory and radar, neutron, thermal, altimeter reflectance, and Lunar CRater Observation and Sensing Satellite (LCROSS) observations suggest volatiles are present in cold traps attributed to permanently shadowed regions (Watson et al., 1961; Ingersoll et al., 1992; Nozette et al., 1996, 2001; Margot et al., 1999; Feldman et al., 2000; Campbell et al., 2003; Colaprete et al., 2010; Mitrofanov et al., 2010; Paige et al., 2010; Spudis et al., 2010; Siegler et al., 2011; Hurley et al., 2012; Zuber et al., 2012). Conversely, some nearby topographic highs adjacent to permanently shadowed regions remain illuminated for a majority of the lunar year, thus providing a benign thermal environment (220 K ± 10 K) and access to solar energy for extended periods of time, making these regions prime locations for long duration missions and sustainable lunar outposts (Goddard and Pendray, 1970; Burke, 1985; Heiken et al., 1991; Shevchenko, 1999). Using images from the Lunar Reconnaissance Orbiter Camera (LROC), localized regions that remain persistently illuminated are identified and characterized.

2. Previous studies

Previous studies investigated both permanently shadowed and persistently illuminated regions with satellite imaging and simulations based on digital elevation models (DEMs) (Shoemaker et al., 1994; Nozette et al., 1996; Bussey et al., 1999, 2005, 2010; Margot et al., 1999; Garrick-Bethell et al., 2005; Noda et al., 2008; Bryant, 2009, Mazarico et al., 2010). In 1994, the Clementine spacecraft orbited the Moon for 71 days (19 February to 3 May 1994) where it collected UVVIS images of the polar regions with a ground sampling distance range of 250–500 m (Nozette et al., 1994; Shoemaker et al., 1994; McEwen and Robinson, 1997). Using this collection of images, Shoemaker et al. (1994) estimated that at least 30,000 km^2 of the south polar region remains in persistent shadow. Nozette et al. (1996) created composite Clementine images by registering and summing more than 50 UVVIS images collected over one lunar day for each pole. From these first-order illumination maps, they were able to identify persistently illuminated regions near both poles. Bussey et al. (1999, 2005) later revisited the UVVIS dataset and were able to further quantify the illumination conditions over each lunar day observed by

* Corresponding author. Fax: +1 480 965 8885.
E-mail address: espeyerer@ser.asu.edu (E.J. Speyerer).

0019-1035/$ - see front matter © 2012 Elsevier Inc. All rights reserved.
http://dx.doi.org/10.1016/j.icarus.2012.10.010

Clementine. Additionally, elevation models derived from Earth-based radar interferometry combined with ray tracing algorithms also provided estimates of the area in permanent shadow and identified persistently illuminated massifs near both poles in regions visible from Earth (Margot et al., 1999; Garrick-Bethell et al., 2005; Bryant, 2009). Recently, refined estimates of permanently shadowed regions and areas of persistent illumination were derived from more complete elevation models provided from the Laser ALTimeter (LALT) instrument onboard the Kaguya spacecraft and the Lunar Orbiter Laser Altimerer (LOLA) onboard the Lunar Reconnaissance Orbiter (LRO) (Noda et al., 2008; Bussey et al., 2010; Mazarico et al., 2010). Although the accuracy of these models increases with higher spatial resolution and more accurate spatial-referencing, direct imaging provides a tool that captures the actual surface lighting conditions of these regions of interest at a given moment in time.

One of the primary scientific objectives of LROC is to identify regions of permanent shadow and extended illumination using its two imaging systems (Robinson et al., 2010). As of 15 September 2012, LROC acquired 24,270 Wide Angle Camera (WAC) observations and 31,673 Narrow Angle Camera (NAC) images within 2° of the poles. Comparatively, the orbital period (~5 h) and mission duration of the Clementine spacecraft limited previous image-based illumination studies to 59 individual south pole images and 53 north pole images collected with a temporal spacing of ~10 h (Nozette et al., 1996; McEwen and Robinson, 1997; Bussey et al., 1999, 2005). The LRO spacecraft and LROC provide the ability to acquire an image dataset with shorter temporal gaps (every orbit; 1.9 h), over all seasonal lighting conditions (i.e. from minimum to maximum subsolar latitude), and at fine ground sampling distances (100 m and 0.5–2.0 m). We reduced a subset of these LROC images into movie sequences, multi-temporal illumination maps, illumination profiles, and high resolution mosaics to locate and characterize the lighting conditions of the poles over a lunar year. From the LROC dataset, we investigated the impact of local topography on the illumination conditions and located small regions of extended illumination, which will impact planning and design of future human and robotic missions to the lunar poles.

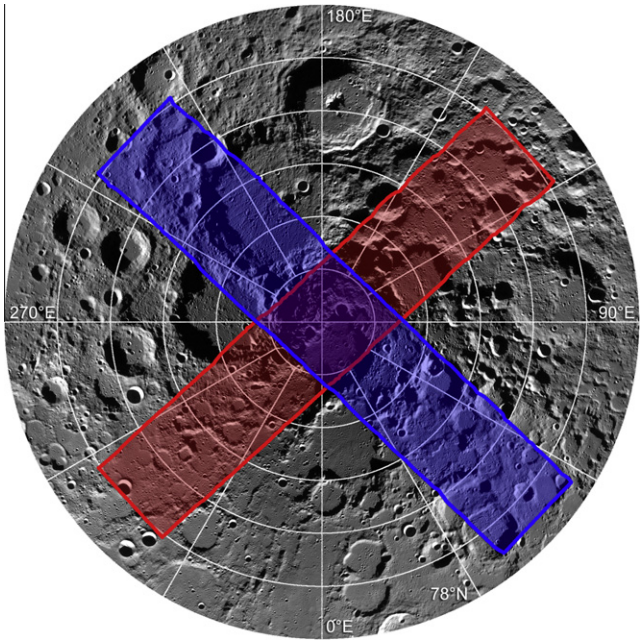

Fig. 1. The LRO mapping orbit and the 90° field of view of the WAC enables repeat coverage of both polar regions as shown by these WAC footprints (red: M121343590M and blue: M121906848M) acquired 156 h apart. The footprints are overlaid on a LROC WAC mosaic of the north polar region.

Table 1
Temporal coverage of LROC WAC observation of both polar regions.

	# Of WAC observations	Mean frequency		Longest temporal gap	
		Orbits	Hours	Orbits	Hours
N. pole (no fill)	3548	1.27	2.38	69	129.95
N. pole (temporal fill)	3782	1.19	2.25	5	9.41
S. pole (no fill)	3807	1.18	2.22	70	131.83
S. pole (temporal fill)	4036	1.12	2.10	4	7.53

3. Broad-scale, multi-temporal mapping

The 50 km mapping orbit enables LROC to acquire images of each pole every 1.9 h during nominal spacecraft and instrument operations (average time between polar WAC observations is 2.1 h due to spacecraft anomalies and operations of other instruments) (Tooley et al., 2010). The orbital velocity and lunar rotation rate results in the solar azimuth shifting approximately 1° of longitude between consecutive orbits. Over each pass of the north and south pole, the WAC images the terrain from 80° poleward to 90° and back to 80° on the opposite side (Fig. 1). The 90° field of view of the WAC (in monochrome mode) allows imaging of a ~100 km wide swath with a ground sampling distance of 100 m. This imaging strategy enables the WAC to observe the illuminated terrain on the day side as well as locate small illuminated regions beyond the terminator (day/night boundary) that remain persistently illuminated over a lunar year. Repeat coverage over the polar regions enables illumination movie sequences, multi-temporal illumination maps, and illumination profiles that delimit and quantify regions of permanent shadow and persistent illumination.

Over one lunar year (12 complete lunations or solar cycles; 15 February 2010 to 5 February 2011), the WAC acquired 3548 and 3807 observations of the north and south polar regions, respectively. During this period, occasional observations were not acquired on some orbits due to instrument and spacecraft anomalies and off-nadir polar observations from other instruments. For example, Miniature Radio Frequency (Mini-RF), a technology demonstration on LRO (Nozette et al., 2010), collected an S-band dataset of both poles that as a consequence decreased the frequency of LROC WAC image acquisition to alternating orbits from June until August 2010 resulting in a temporal spacing of 3.8 instead of 1.9 h. A second Mini-RF mapping campaign for the north polar region was conducted in November 2010 (Bussey, 2011), which accounts for the ~250 fewer observations of that pole during the 1 year period examined in this study. To fill the larger gaps in temporal coverage due to instrument and spacecraft anomalies, WAC observations with virtually identical lighting geometries acquired at other times during the mission were added to the image sequence. In all, 234 and 229 observations of the north and south polar regions were added, which eliminated many of the temporal gaps and reduced the longest gap in image acquisition to five orbits (9.4 h) for the north and four orbits for the south polar region (7.5 h) (see Table 1 and Fig. 2).

3.1. Illumination movie sequences

Each of the WAC observations in the series described above was radiometrically calibrated and map projected (polar stereographic) at a pixel scale of 100 m using a nearest neighbor interpolation. The nearest neighbor interpolation was chosen over averaging algorithms to prevent further smearing of pixel values along the

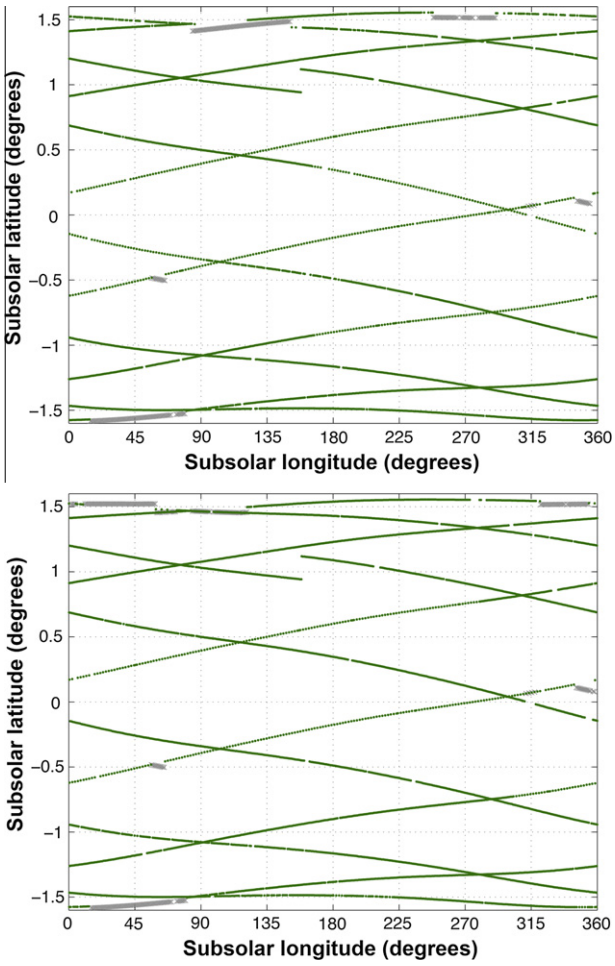

Fig. 2. Profile of LROC WAC observations of the north (top) and south (bottom) polar regions. Green points denote the subsolar point at time when WAC observations were acquired of the polar region between 15 February 2010 and 5 February 2011, while gray points indicated the subsolar point when images from other time periods were used to eliminate large gaps in the temporal coverage caused by spacecraft anomalies and other instrument operations.

terminator that may alter the classification of the illumination state for a given pixel. An improved WAC distortion model (Speyerer et al., 2012), a 30 m DEM provided by the LOLA team (Smith et al., 2010), and improved spacecraft ephemeris derived from a combination of radio tracking, orbit crossovers, and Earth-based laser ranging (Mazarico et al., 2011) enabled accurate map projection to within one mapped pixel (100 m) for each WAC observation over the entire time period examined. Once projected, the images were then arranged in a time-sequence to enable a visualization of the dynamic lighting conditions at both poles as the Sun grazes across the horizon each lunar day and the subsolar latitude migrates between 1.58°S and 1.55°N over the lunar year studied (Fig. 3 and S1 and S2 in Supplementary materials). This image set was then compiled into illumination maps and profiles for each pole to identify regions of extended illumination.

3.2. Illumination maps of the lunar poles

To generate maps that provide illumination statistics, the individual map-projected images (Fig. 4A) were first converted into binary images delimiting pixels that are illuminated from those in shadow (1 = sunlit; 0 = shadow). Due to of the large size of the LROC WAC image dataset used in this study (>7800 images; $\sim 9.0 \times 10^9$ mapped pixels within 2° of the poles), an automated algorithm that classified the illumination state of the pixel was used. Because of scattered light effects (both natural and instrumental; Fig. 4B), a standard global threshold alone does not optimally discriminate the terminator because some illuminated pixels have intensities less than nearby areas affected by scattered light. Furthermore, more advanced optimal or adaptive thresholding methods (Gonzalez and Woods, 1992) fail to classify the illumination state of the pixel accurately due to the wide range of valid intensity values in small, localized regions.

To negate the influence of scattered light and better determine the illumination state of a given pixel, we applied a series of spatial filters and a conservative global threshold. First, a 5×5 high pass filter was applied to the map projected WAC image. The filter enhances regions of the image with high contrast boundaries (i.e. small points of light, illuminated crater rims, etc.) while attenuating areas with a low frequency signal (i.e. regions in shadow, areas receiving diffuse illumination from nearby illuminated terrain, and areas affected by instrumental scattered light). A threshold was applied to the high pass filtered image to create a binary image (Fig. 4C) that delimits areas with high contrast signatures (ones) from areas with little contrast among surrounding pixels (zeros). Next, a 5×5 pixel low pass filter was applied to the binary high pass filtered image to average out rapid change in the binary values by filling in the high contrast illuminated terrain identified in Fig. 4C. A threshold was then applied to the low pass filtered image to create a new binary image (Fig. 4D) that delimits illuminated and shadowed terrain with ones and zeros respectively. The threshold was chosen such that a majority of the neighboring pixels must be true (i.e. illuminated) thus ensuring that the illuminated area does not "grow" beyond the terminator boundary as a result of the low pass filter. Finally, to identify smooth illuminated surfaces, a conservative global threshold was applied on the original image (Fig. 4E). The threshold was chosen empirically by analyzing several hundred images acquired throughout the mission and identifying the lowest threshold (DN value) that would not falsely include regions in shadow or under the influence of scattered light. The two binary images that are a result of the filtering and the global thresholding to the original image (Fig. 4D and E) were then joined into a single binary image (Fig. 4F) that more accurately delimits illuminated and shadowed terrain in each WAC observation. A subset of observations was manually inspected to ensure the algorithm accurately delimited the illuminated and shadowed terrain.

Due to inclination drift of the LRO orbit, the orbit track wanders around the geographic poles. Furthermore, the Moon's non-uniform gravitational field causes the altitude of LRO to vary between station-keeping maneuvers (Tooley et al., 2010); the standard deviation of the altitude fluctuation is about 6.5 km over the polar regions. These effects limit the extent of near complete multi-temporal coverage (>90%) to within 1° of the poles and therefore, only areas in these zones were analyzed (Fig. 5A). Given these constraints, an illumination map was derived by stacking the binary illumination frames in map space and taking the ratio of the number of instances the mapped pixel was illuminated in the time sequences (15 February 2010 to 5 February 2011) by the number of times the location was imaged with the LROC WAC during the same period (Fig. 5B).

In addition to the ratio-based illumination maps, a time-weighted map was derived. In this technique, biases that were introduced by non-equally spaced observations were minimized. The illumination state of pixels in images acquired during periods of less frequent LROC WAC observations, such as during Mini-RF polar mapping campaign, were weighted twice as much as the illumination state of pixels from images acquired during nominal operations when observations were twice as frequent. In the time-weighted maps, areas not within the field of view were

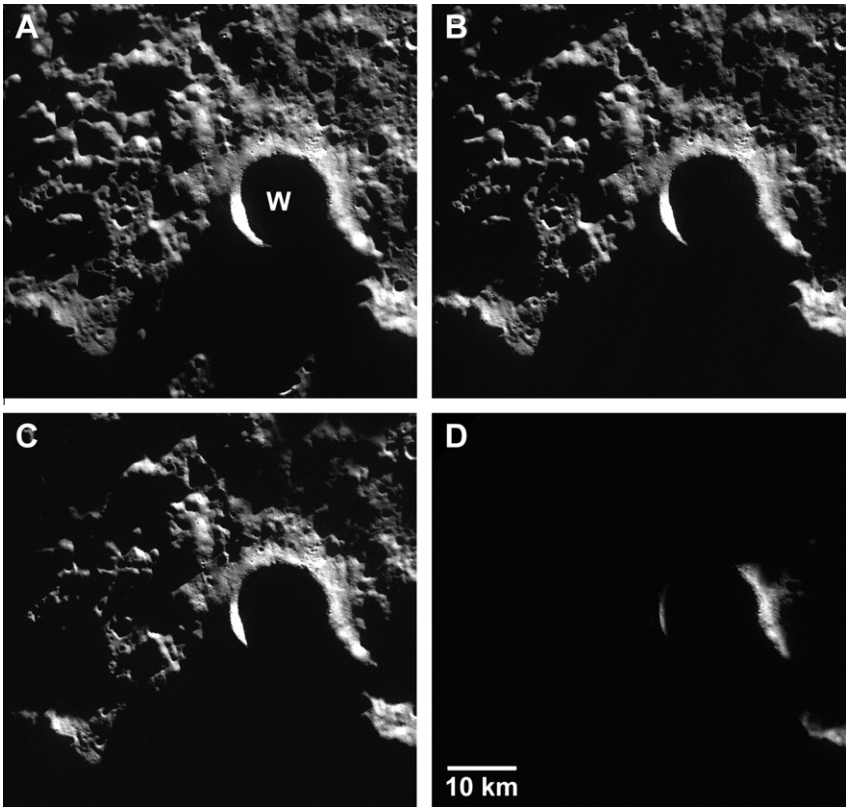

Fig. 3. Subset of map projected LROC WAC images of the same region around Whipple crater (marked with W; 89.140°N, 14.5°E) with identical solar azimuths (150°E), but varying subsolar latitudes (A) M126067558M, subsolar latitude: 1.52°N; (B) M131163569M, subsolar latitude: 0.53°N; (C) M133701038 M, subsolar latitude: 0.24°S; (D) M141347884M, subsolar latitude: 1.49°S.

linearly interpolated based on the preceding and subsequent observation where image data was available for the specific mapped pixel (Fig. 6). Due to the inclination of the orbit and altitude variations, some regions near both poles were not imaged for many consecutive orbits creating temporal gaps (Fig. 7A). However, persistently illuminated regions along Shackleton crater near the south pole were imaged more frequently with the largest gap in temporal coverage lasting fewer than 45 h over the complete lunar year studied. Likewise, portions of the rim of Peary crater and the persistently illuminated regions near Hinshelwood crater near the north pole had limited temporal gaps lasting less than 40 h and were imaged in over 93% of all WAC observations during that period. A similar averaging method was used by Bussey et al. (1999) to create quantitative illumination maps using Clementine images of the north polar region. The LROC WAC time-weighted maps (Fig. 7B) provide a useful tool for analyzing the percent of the lunar year a given region was illuminated and the longest, single period of time the region was in shadow.

The resulting ratio (Fig. 5B) and time-weighted (Fig. 7B) illumination maps were produced for both poles at a pixel scale of 100 m over a complete lunar year and are thus a factor of two higher resolution than previously published maps derived from 71 days of Clementine image data – 500 m/pixel (Nozette et al., 1996; Bussey et al., 1999, 2005) and simulations based on lower resolution DEMs derived from orbital observations: Kaguya/LALT – 474 m/pixel (Noda et al., 2008; Bussey et al., 2010) and LRO/LOLA – 240 m/pixel (Mazarico et al., 2010). Each map provides a unique look at the illumination environment near the polar regions. The ratio-based illumination map provides statistics without interpolation, while the time-weighted maps mitigate biases caused by non-uniform temporal sampling. The higher spatial resolution data obtained by LROC WAC enables the identification of smaller areas down to 0.01 km^2 that remain illuminated for extended periods of time that may go undetected with lower resolution images and simulations based on lower resolution DEMs. Likewise, the higher spatial resolution may actually result in a lower illumination estimate on a pixel-by-pixel basis as illumination marches around a small peak (Table 2). To account for these two competing effects, we examined pixel-by-pixel illumination (Figs. 5B and 7B) and regional illumination of small areas (see Section 5). The latter method consists of recording an $m \times n$ area as illuminated, if any pixel in the denoted region was illuminated. The size of the $m \times n$ area was chosen based on local trafficability of the region.

For this study, we focused on the illumination conditions within 1° of the poles where WAC temporal coverage was most complete. However, the WAC illumination maps presented in Figs. 5B and 7B extend out to 88° to provide illumination context for the region albeit with less temporal frequency (Figs. 5A and 7A). Direct investigation of these illumination maps revealed several small regions that received direct sunlight for an extended period (between 15 February 2010 and 5 February 2011). For example, near the south pole a 0.01 km^2 (100 m × 100 m) region, on the edge (89.740°S, 201.2°E) of Shackleton crater, was illuminated in 71.6% of images acquired during the year (time-weighted illumination: 71.7%), while a 0.01 km^2 portion of a massif (89.418°S, 221.3°E), located about 10 km off the rim of Shackleton crater, was illuminated in 64.2% of WAC frames (time-weighted illumination: 63.3%). The north pole illumination maps reveal two highly illuminated crater rims: a 0.01 km^2 region (89.370°N, 127.6°E) of Whipple crater was identified as illuminated in 63.3% of WAC frames acquired during the lunar year (time-weighted illumination: 63.9%) and a similarly sized region on the rim (89.655°N, 308.0°E) of Hinshelwood crater was illuminated in 53.9% of the WAC observations acquired during the lunar year (time-weighted illumination: 55.1%). While many of the persistently illuminated peaks were identified in Clementine images (Nozette et al., 1996; Bussey et al., 1999, 2005) and in later

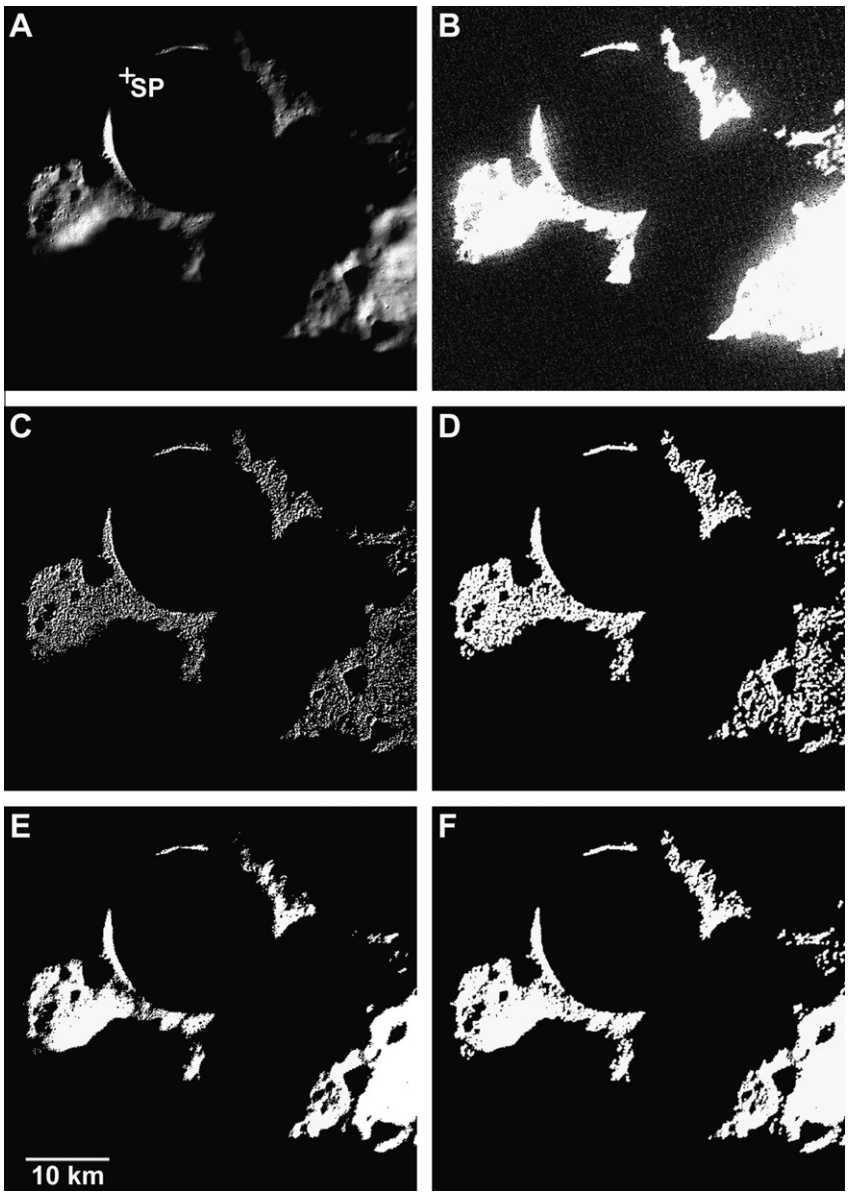

Fig. 4. Technique used to delimit illuminated and shadowed terrain: (A) Original map projected LROC WAC image (M121129924M) near the south pole (marked with SP). (B) Original image with hard stretch to illustrate the scattered light effect; (C) Binary image after applying high pass filter; (D) Binary image after applying low pass filter; (E) Result of conservative global threshold; and final illumination frame produced (F) from merging (D) and (E).

studies using both Earth-based and altimeter derived DEMs (Garrick-Bethell et al., 2005; Noda et al., 2008; Bryant, 2009, Bussey et al., 2010; Mazarico et al., 2010), LROC WAC derived illumination maps provide a higher spatial and temporal resolution dataset to aid in identifying future landing sites and outpost locations for both robotic and human explorers.

3.3. WAC illumination profiles

In addition to multi-temporal illumination maps, profiles depicting the illumination state at each lighting condition in which an LROC WAC observation was acquired were produced for high priority targets, such as persistently illuminated regions (Fig. 8). A benefit of presenting the lighting condition in this manner is that unlike a single multi-temporal illumination map, these plots enable predictions of the illumination state for a region at a given time, based on the location of the Sun with respect to the Moon (subsolar latitude and longitude). In the example shown in Fig. 8, point A is in shadow due to the fact that at the same subsolar longitude the area was in shadow when the Sun was lower on the horizon (i.e. higher subsolar latitude in the north polar region). In the case of point C, the region is sunlit because at the same subsolar longitude the region was illuminated when the Sun was lower on the horizon (lower subsolar latitude in the north polar region). However, the illumination state is unknown in the case of point B where the state is in transition at the particular subsolar longitude and subsolar latitude range. Additional LROC WAC observations acquired outside the one lunar year examined in this study can be added to these illumination profiles to increase the accuracy of the prediction and reduce cases of uncertainty by minimizing sampling gaps, but have been omitted in this example for clarity.

4. Meter scale mapping and analysis

4.1. Mapping regions of direct and indirect illumination

Due to the inherent narrow field of view (2.85° each and 5.7° combined) of the NACs broad scale multi-temporal mapping is

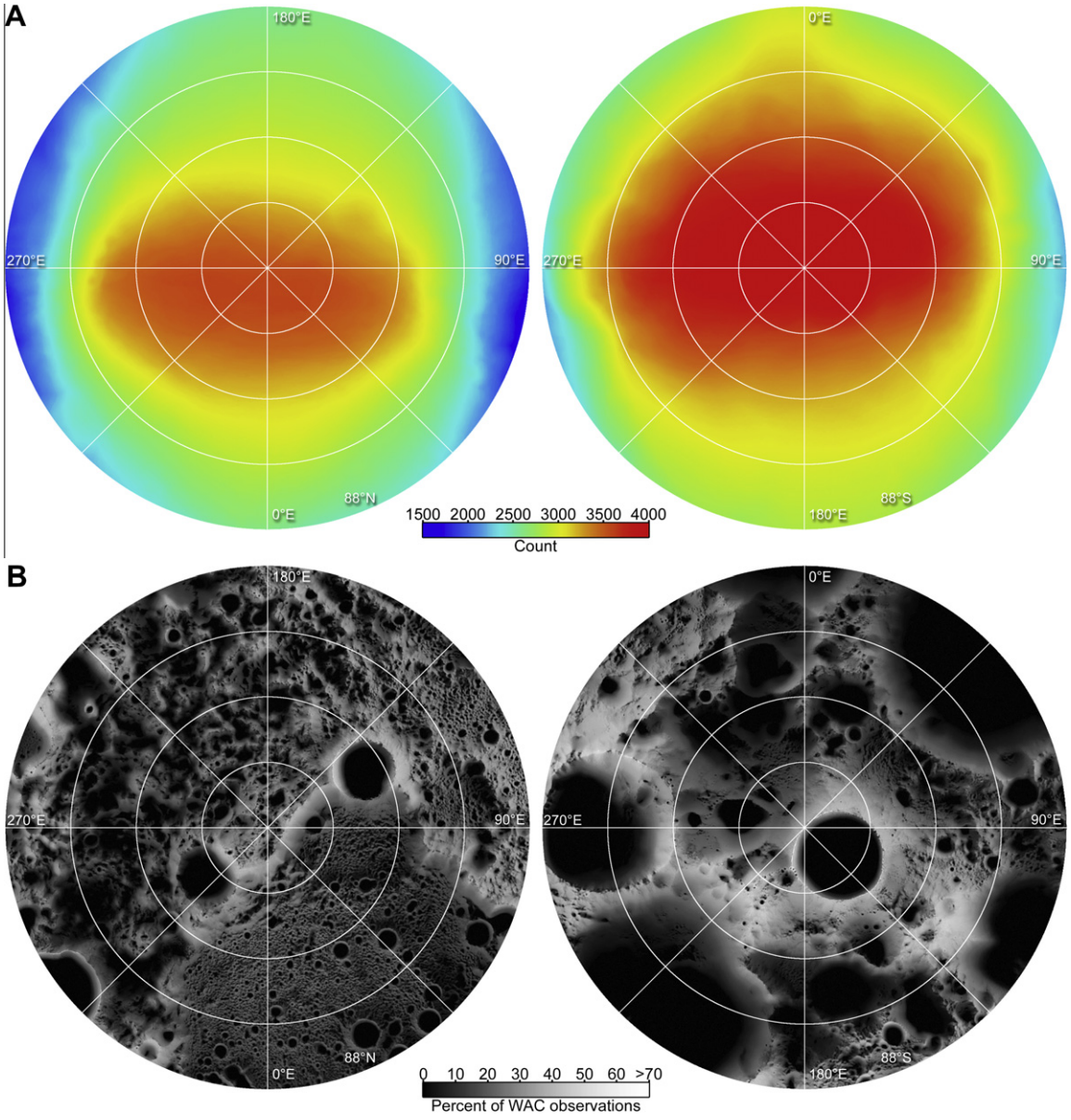

Fig. 5. Orbit inclination and varying altitude prevent some WAC images from spanning the entire region within 2° of the poles as shown by the coverage maps (A) derived from the 3782 and 4036 WAC observations acquired of the north and south pole during a lunar year (15 February 2010 to 5 February 2011). (B) First order illumination map derived by the taking the ratio of the number of times a mapped pixel was illuminated by the number of instances the mapped pixel was imaged.

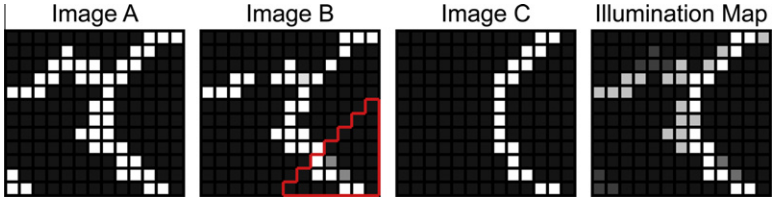

Fig. 6. Example of three binary illumination images used to make an illumination map. The red box in 'Image B' denotes pixels outside the field of view of that observation. In creating time-weighted illumination maps, this region is linearly interpolated based on the proceeding and following observation of the mapped pixel.

limited (Robinson et al., 2010). However, around the summer solstice for each pole, when the Sun is highest along the horizon and shadows are minimized, the NAC acquires hundreds of images that are used to create meter scale maps of the illuminated terrain at the each pole (85.5–90°N/S) (Fig. 9). After the solstice, the NAC continues to remap the same regions under varying lighting conditions. Most of the NAC polar observations are summed (averaged) by a factor of two in the cross-track direction to increase the signal-to-noise ratio of the image at the cost of decreasing spatial resolution by 2× in the cross track direction.

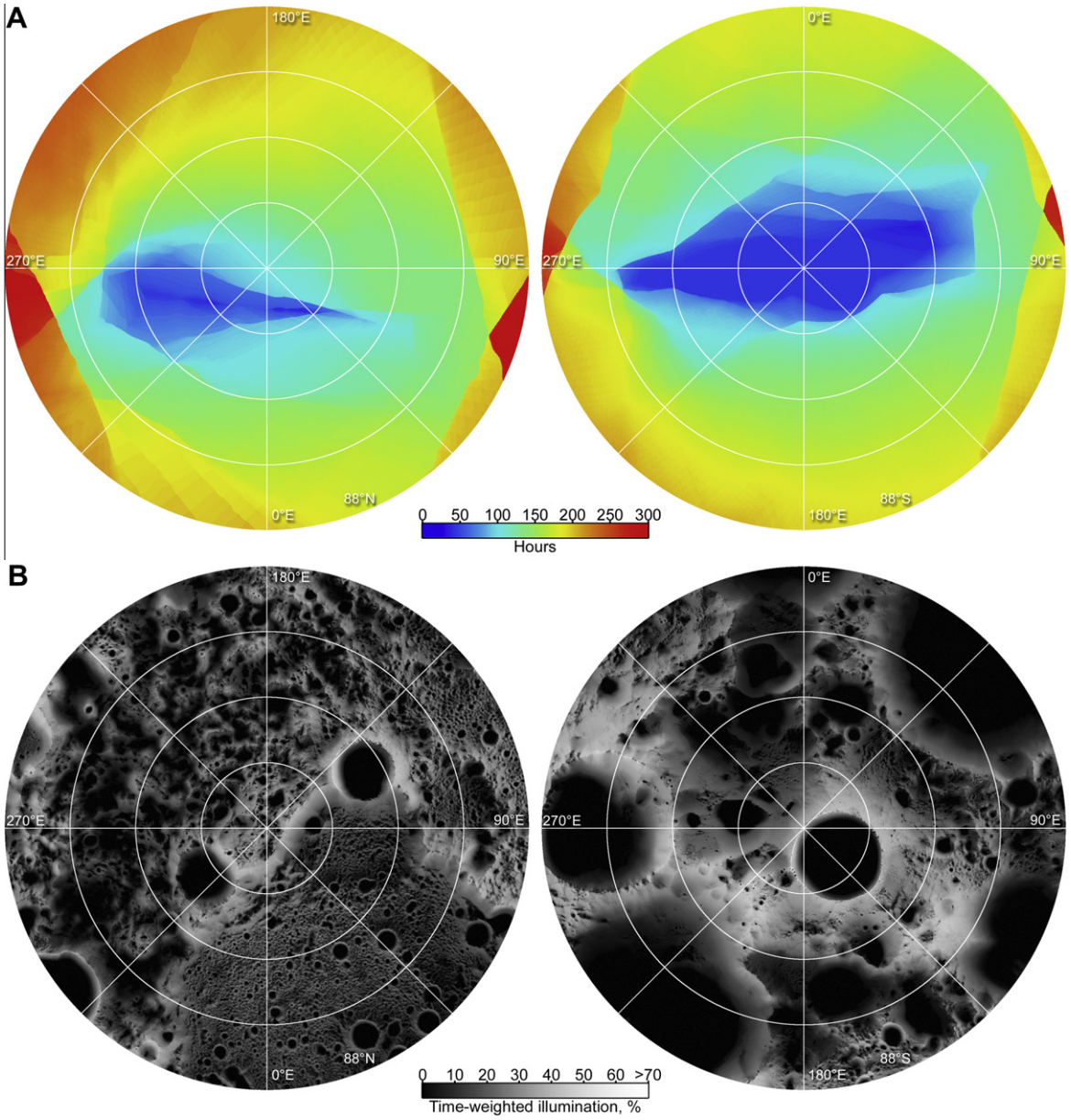

Fig. 7. Time-weighted illumination maps of the both polar regions. (A) When the orbit track drifts away from the pole, some regions fall outside the field of view of the LROC WAC creating gaps in the temporal coverage, which is quantified here. (B) Time-weighted illumination map reduce the effect of non-linear temporal sampling by linearly interpolating between observations (Fig. 6).

Table 2
Comparison of highly illuminated points within 1° of the pole.

Study	Pixel scale (m)	North pole	South pole
Noda et al. (2008)	474	87% (89.4°N, 127.3°E)	84% (89.8°S, 207.5°E)
Bussey et al. (2010)	474	–	82% (89.44°S, 218.2°E)
Mazarico et al. (2010)	240	84.56% (89.37°N, 126.80°E)	89.01% (89.45°S, 222.69°E)
This work (ratio-based)	100	63.3% (89.370°N, 127.6°E)	71.6% (89.740°S, 201.2°E)
This work (time-weighted)	100	63.9% (89.370°N, 127.6°E)	71.7% (89.740°S, 201.2°E)

In addition to observing regions in direct illumination, long exposure NAC observations reveal features in permanent shadow under optimal conditions when light from sloping topographic facets illuminate nearby shadowed terrain (Fig. 10). However, some regions still remain concealed due to being doubly shadowed, i.e. not receiving any direct or single-reflection indirect illumination. The ability to image shadowed terrain is dependent on the amount of secondary illumination and the increased exposure time of the NAC observation. As a result of the increased exposure time, the spatial resolution of the NAC images in the down track direction is reduced. Mapping both the direct and single-reflection indirect illuminated terrain aids in identifying safe landing sites, traverse options, and potential cold traps for future human and robotic explorers.

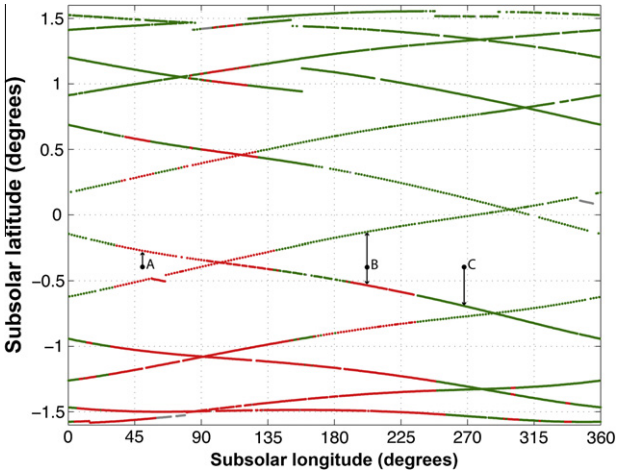

Fig. 8. Illumination profile of 0.01 km^2 mapped pixel (89.655°N, 308.0°E) on the rim of Hinshelwood crater. Green points indicate the surface was illuminated for the given subsolar point, red points indicate the mapped pixel is in shadow, and gray points identify times when the mapped pixel was outside the field of view of the LROC WAC during the polar pass. Profiles can be used to predict, given a subsolar point, whether the region will be illuminated (point C) or in shadow (point A). Given the available data in this profile, the illumination state of B is unknown.

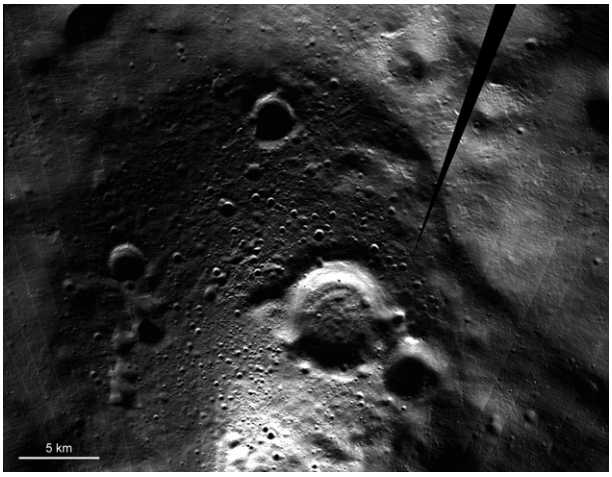

Fig. 10. Mosaic of long exposure (24.2 ms) NAC images covering the permanently shaded region inside Shoemaker crater. Sunlight is coming from the top of the image and reflecting off the crater rim just out of view near the bottom of the image. The diffuse, reflected sunlight is indirectly illuminating a majority of the crater floor. Some regions remain doubly shadowed (i.e. not receiving direct or first-order, indirect illumination). The image center is at 87.98°S, 46.2°E.

4.2. Validation of broad-scale illumination maps

Although the NAC temporal coverage is relatively limited, the high spatial resolution (ground sampling distance up to 0.5 m) proves useful in validating previous illumination studies that used lower resolution topographic models (Noda et al., 2008; Bussey et al., 2010; Mazarico et al., 2010). Fig. 11 shows the results of a simulation of the illumination conditions near the south pole using a 240 m/pixel LOLA DEM compared with a LROC WAC and NAC images acquired at the same time as the simulation (18 March 2011 15:59 UTC). While the LOLA simulation accurately identifies the terminator boundary across rim of Shackleton crater, it fails to resolve some nearby local depressions and small craters that remain in shadow. Meanwhile, the WAC image, which was processed using the algorithm described in Section 3.3, more accurately portrays the major shadow boundaries and many of the $\geqslant$100 m scale shadowed features.

Inspections of other NAC images revealed cases where small massifs and crater rims were illuminated when previous models predicted the area to be in shadow (Fig. 12). A lighting simulation constructed from a 474 m/pixel LALT DEM predicted that a region (Point B in the study) is eclipsed by the horizon for a 276 h period (Bussey et al., 2010). However, NAC images (Fig. 12) acquired with subsolar points within the eclipsed period (1.45°N, 62.0°E and 1.55°N, 61.5°E) revealed a small illuminated peak within the region, thus reducing the longest period Point B is eclipsed to fewer than 180 h. Conversely, NAC images also revealed regions in shadow at times in which models showed them illuminated (i.e. small craters in Fig. 11).

Due to the extreme incidence angles near the poles, lighting simulations are sensitive to the quality of the input DEM. The first lighting simulations using DEMs from Earth based radar observations were limited due to incomplete topographic coverage of the polar far side (Garrick-Bethell et al., 2005; Bryant, 2009). Recent

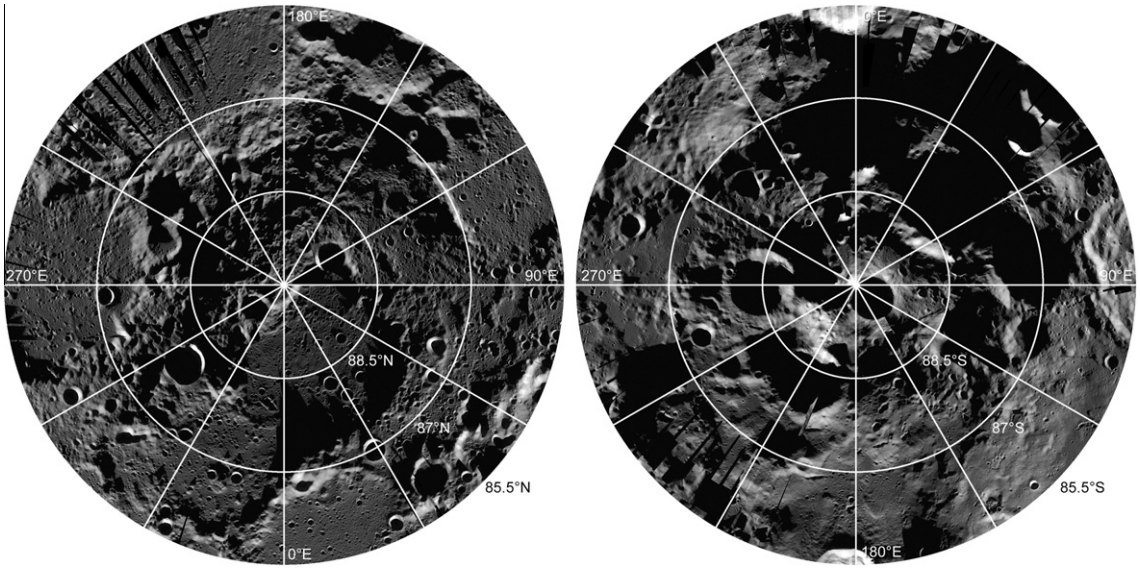

Fig. 9. Two m/pixel NAC mosaics of the polar regions (85.5°–90°N/S).

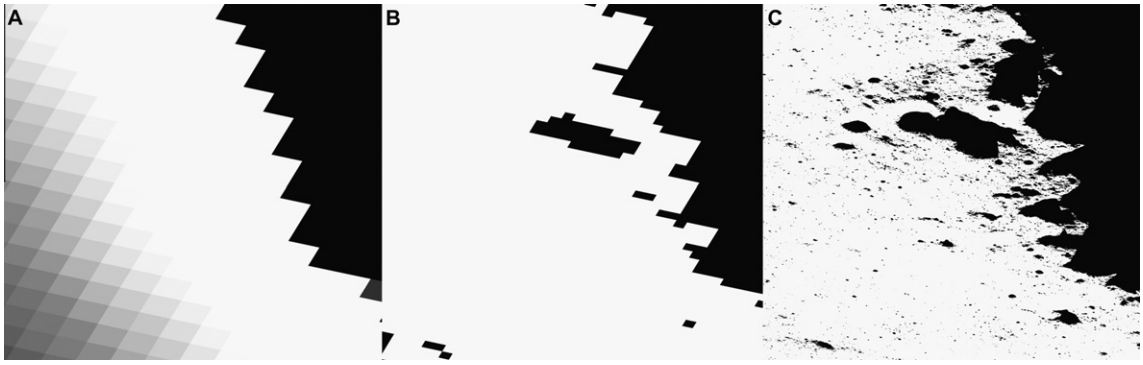

Fig. 11. LOLA simulation vs. LROC image comparison: (A) LOLA lighting simulation (Mazarico et al., 2010) based on a 240 m/pixel DEM; (B) binary WAC illumination image based on M155103029M; (C) NAC image (M155103207R) with hard stretch to delimit the illuminated and shadowed terrain. Each image is centered at 89.972°S, 344.5°E.

studies that have used DEMs generated from laser altimeters on LRO and Kaguya are more robust and accurately simulate the lighting environment (Noda et al., 2008; Bussey et al., 2010; Mazarico et al., 2010). While there are occasional residual errors, these illumination models can simulate the lighting conditions for periods where image data is missing and predict future lighting conditions for a particular area at any Sun angle. In fact, simulations provided by the LOLA team are used in planning and targeting NAC observations at the LROC Science Operations Center. Finally, lighting simulations can also estimate the illumination condition at different heights above the surface, which cannot be achieved with direct inspection of image data. This ability is important for planning lander and rover missions that use a small mast to increase the amount of time the solar panels are illuminated (Burke, 1985; Bryant, 2009; Mazarico et al., 2010).

5. Discussion

Previous studies focused on the identification of discrete points in LALT and LOLA DEMs that receive extended, direct illumination (Table 2) (Noda et al., 2008; Bussey et al., 2010; Mazarico et al., 2010), because they are prime targets for future polar missions due to their persistent access to solar energy and proximity to permanently shadowed regions. Bussey et al. (2010) identified two points about 10 km apart (89.68°S, 194.0°E and 89.44°S, 218.2°E) in the LALT DEM that were collectively illuminated for 94% of the year. Further work by Mazarico et al. (2010) investigated the illumination conditions 10 m above the surface. They found that this small altitude difference increased the amount of time the point was illuminated, and in one example (89.45°S, 222.69°E) reduced the longest period in shadow from 414 to 66 h.

The results presented in Section 3.2 show that small regions (0.01 km^2) near the lunar poles remain illuminated for less than 72% of the year. However, with the high spatial resolution of the LROC images, we investigated the illumination conditions of varying spatial extents by testing the illumination status of groups ($m \times n$ size) of map-projected pixels (Figs. 13 and 14 and Tables 3 and 4). From this analysis, we found that roving over a small region increases the percentage of time an asset was illuminated and reduces the longest time period in shadow. This technique is also thermally advantageous since it reduces the time periods the explorer or mobile station is in shadow thus avoiding large temperature gradients experienced when crossing the terminator for extended periods of time (Heiken et al., 1991).

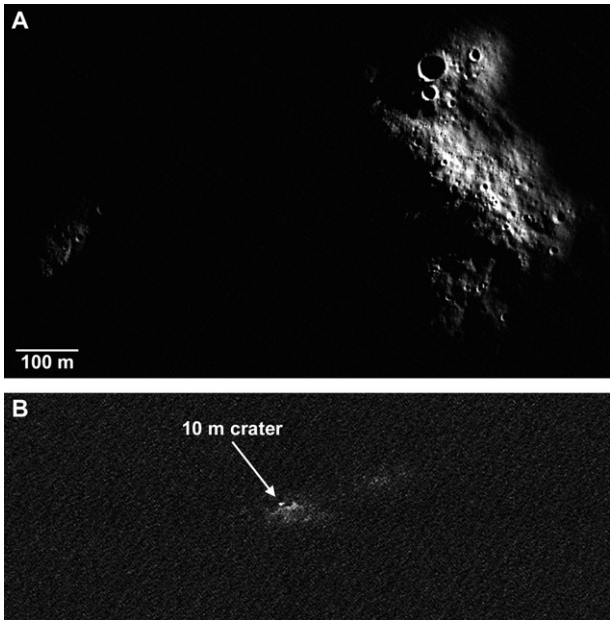

Fig. 12. Small illuminated peaks in an area previously modeled with a 474 m/pixel Kaguya DEM to be in shadow for a 276 h period (Bussey et al., 2010). LROC NAC images (A) M126688662R and (B) M185374654R with subsolar point of 1.45°N, 62.0°E 1.55°N, 61.5°E respectively.

5.1. Shackleton crater

Shackleton is a 21 km diameter crater near the south pole (89.655°S, 129.2°E) that is superimposed on an irregularly shaped platform-like massif, and its interior is perpetually in shadow (Bussey et al., 1999; Margot et al., 1999; Spudis et al., 2008; Siegler et al., 2011; Zuber et al., 2012). Based on the WAC images acquired of Shackleton crater we estimate a majority of its interior, 235 km^2, remains in shadow during the lunar year examined, which is consistent with LOLA simulations derived from the 240 m/pixel DEM that found that 233 km^2 remained in shadow (Mazarico et al., 2010). This large permanently shadowed region is of interest to both the science and exploration community due to its potential for harboring volatiles collected over long periods of time. Wilhelms et al. (1979) identified Shackleton crater as being Eratosthenian in age emplaced on older, pre-Nectarian basin material. Further work by Spudis et al. (2008) refined the age estimate of Shackleton to ~3.6 Gyr, which is consistent with its generally rounded features and lack of impact melt. More recently, Zuber et al. (2012) produced shaded relief maps derived from a 10 m/pixel LOLA DEM and counted craters in illuminated and permanently shaded regions, which produced a model age of ~3.69–3.60 Gyr for Shackleton crater. Additional analysis of LOLA reflectance

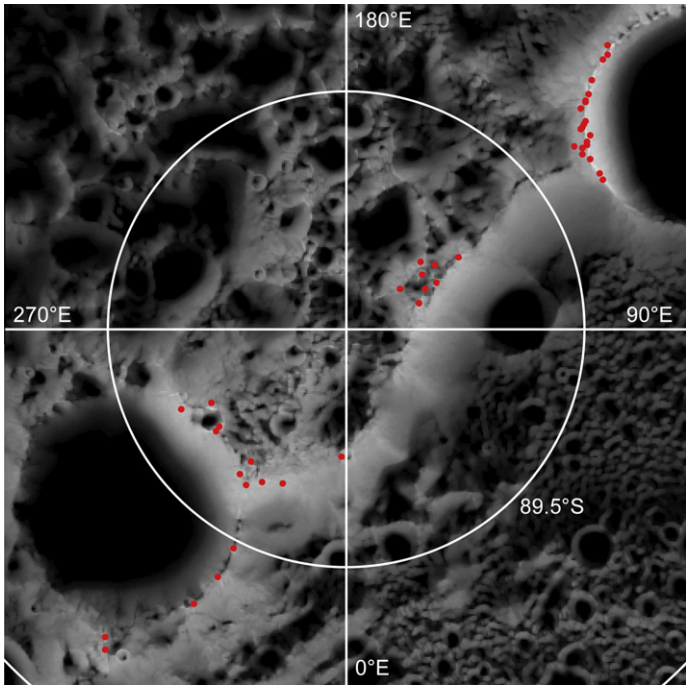

Fig. 13. LROC WAC illumination map of the north polar region with points denoting local illumination maxima. Illumination statistics for each point are available in Table 3.

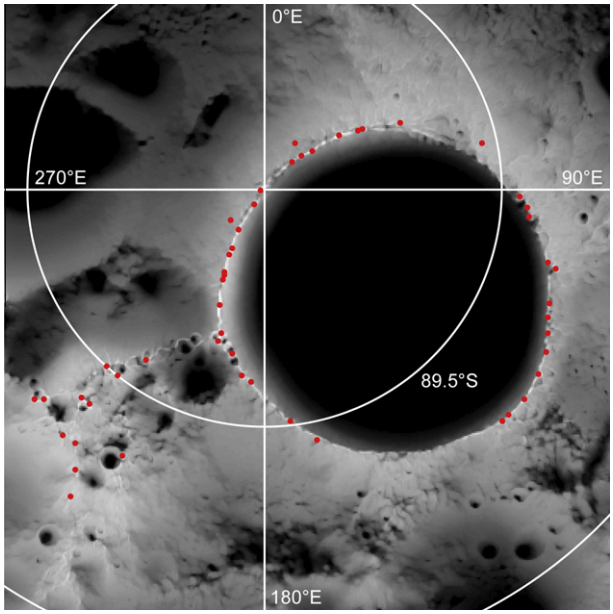

Fig. 14. LROC WAC illumination map of the north polar region with points denoting local illumination maxima. Illumination statistics for each point are available in Table 4.

measurements revealed that Shackleton crater has a brighter floor than the surrounding terrain. Zuber et al. (2012) speculated that this higher reflectance could be explained by a maturity contrast or a micrometer thick surface layer of ice covering ~20% of a LOLA sample area.

Using just over 50 Clementine images with a ground sampling distance of 500 m, Nozette et al. (1996) and later Bussey et al. (1999) concluded that some portions of the rim of Shackleton crater remain illuminated for a majority of the lunar year. Later DEM based models identified similar findings (Garrick-Bethell et al., 2005; Noda et al., 2008; Bryant, 2009, Bussey et al., 2010; Mazarico et al., 2010). With the finer special resolution of the LROC WAC (100 m/pixel) and extended multi-temporal coverage, we identified small illuminated peaks (~0.01 km^2) on the rim of Shackleton crater that collectively remain illuminated for extended portions of a year. From the illumination map presented in Fig. 5B, a small 0.01 km^2 region (89.740°S, 201.2°E) was identified as being illuminated in 71.6% of the LROC WAC images acquired during the lunar year examined with its longest period of eclipse lasting 145 h. To prolong access to solar energy, future missions to Shackleton crater may opt to erect a boom with a solar panel affixed to the top, actively traverse along illuminated portions of the crater rim, and/or distribute a series of solar panels at ground level across a small region surrounding this persistently illuminated location. To examine the feasibility and potential of the latter two methods, the illumination state of state of several WAC pixels within an $m \times n$ region were analyzed (Table 4 and Fig. 14).

Using this method, we identified a persistently illuminated region on the rim of Shackleton crater that is ideal for a rover capable of traversing along the rim and/or a series of stationary assets such as solar power stations. This region contains three locations that are independently and collectively illuminated for a majority of the lunar year: Station 1 (89.685°S, 196.7°E), Station 2 (89.740°S, 201.2°E), and Station 3 (89.808°S, 205.9°E). Stations 1 and 2, which are located 1.8 km from one another, were collectively illuminated for 86.9% of the year and were both in shadow for a maximum period of 63 h. Meanwhile, Stations 2 and 3, which are located 2.1 km away from each other, remain illuminated for 85.5% of the year and were eclipsed for a maximum period of 60 h. Combined, at least one of the three stations was illuminated for 92.1% of the year and the longest period all three were in shadow was *43* h. Adding a small amount of mobility (~100 m) at each station increases the illumination percentage to 93.8% of the year. Fig. 15 highlights these three outpost stations and outlines prospective traverses between them. Ongoing processing of NAC stereo observations of this region provides detailed elevation models at a scale of 3 m and a vertical accuracy of 1 m to enable prospective explorers to define

Table 3
Persistently illuminated regions near the north pole (points in the table are organized by longitude). With the ability to traverse a short distance or distribute an array of solar cells, an explorer can increase the percentage of the year illuminated and reduce the longest period in shadow. Various size regions ($n \times n$) are examined to show the impact mobility has on illumination. The longest period in shadow is unknown for several locations due to gaps in temporal coverage when the region was transitioning between the shadowed and illuminated state.

ID #	Location		# Of WAC obs.	Longest temporal gap, hours	Ratio-based illumination percentage					Time-weighted illumination percentage					Longest period in shadow, hours				
	Lat.	Lon.			0.01 km^2	0.25 km^2	1.00 km^2	2.25 km^2	4.00 km^2	0.01 km^2	0.25 km^2	1.00 km^2	2.25 km^2	4.00 km^2	0.01 km^2	0.25 km^2	1.00 km^2	2.25 km^2	4.00 km^2
N01	89.840	109.9	3693	91	46.5	62.3	77.4	77.7	78.1	47.3	62.2	78.1	78.5	78.8	467	458	336	336	336
N02	89.816	117.3	3680	93	18.7	30.1	70.7	75.0	80.5	18.5	30.4	70.7	75.3	80.7	4065	2996	450	417	142
N03	89.790	117.6	3669	95	51.1	65.9	72.4	75.4	79.4	51.9	65.4	71.9	75.1	79.4	626	454	322	311	205
N04	89.383	120.3	3442	121	55.6	64.3	68.6	72.0	76.4	54.9	58.4	62.8	66.5	71.2	317	315	296	294	290
N05	89.382	121.7	3428	121	58.1	66.8	72.5	75.4	83.5	58.7	60.7	66.6	69.7	78.1	300	296	290	290	211
N06	89.723	122.8	3620	98	44.7	72.4	75.4	75.8	76.7	45.2	70.4	74.1	74.6	75.7	445	307	247	247	245
N07	89.382	125.0	3411	121	57.1	83.0	84.1	84.8	85.9	58.1	76.7	77.9	78.8	80.0	330	213	213	213	209
N08	89.806	126.0	3662	95	37.0	55.0	59.9	62.1	77.1	37.9	53.7	58.4	60.9	76.8	701	697	433	426	150
N09	89.773	126.1	3643	97	18.6	32.9	56.4	76.1	79.2	19.3	32.7	54.9	75.5	78.5	697	648	584	145	145
N10	89.390	126.7	3412	123	35.9	39.4	84.7	85.8	86.1	37.1	38.0	78.8	79.7	80.2	441	437	211	211	209
N11	89.861	127.3	3684	91	23.9	44.8	62.6	65.3	74.8	25.7	46.1	62.5	65.2	75.3	1289	341	332	332	142
N12	89.370	127.6	3393	127	63.3	83.1	84.9	85.4	85.9	63.9	76.6	78.5	79.2	79.7	303	213	209	209	207
N13	89.382	127.6	3403	125	35.1	46.9	84.9	85.5	86.0	36.4	44.2	78.6	79.4	80.0	443	211	209	209	209
N14	89.366	128.0	3387	129	62.3	83.6	84.7	85.3	85.9	63.8	76.9	78.3	78.9	79.6	298	211	211	209	207
N15	89.352	128.6	3378	129	45.9	54.8	84.5	85.5	86.7	47.5	49.1	77.6	79.0	80.1	392	379	209	209	207
N16	89.393	128.8	3405	125	32.3	35.9	40.5	69.0	85.8	34.3	34.6	39.0	64.1	80.0	669	443	441	209	209
N17	89.359	130.6	3368	131	36.2	48.1	85.4	85.9	86.0	37.7	44.7	78.3	79.0	79.5	445	209	209	209	209
N18	89.355	130.6	3365	131	35.9	83.7	85.5	85.7	86.1	36.7	76.3	78.2	78.7	79.4	441	209	209	209	209
N19	89.348	130.9	3359	131	32.6	85.2	85.4	85.5	86.1	34.7	77.4	78.0	78.4	79.3	440	209	209	209	209
N20	89.341	131.1	3354	131	55.6	82.1	85.5	85.5	85.8	56.7	74.6	77.9	78.2	78.8	332	211	209	209	207
N21	89.792	132.4	3652	95	33.7	39.4	55.3	56.8	61.4	35.9	39.5	53.8	55.5	60.1	454	424	424	424	424
N22	89.330	133.4	3337	133	33.3	48.3	83.9	84.7	85.7	35.2	44.7	76.1	77.0	78.1	456	209	209	209	209
N23	89.314	133.6	3325	135	61.3	77.9	82.8	84.3	85.0	63.2	70.2	74.9	76.4	77.3	–	–	–	–	–
N24	89.312	133.8	3325	135	60.8	74.5	82.5	84.2	84.7	63.7	67.2	74.8	76.3	77.1	–	–	–	–	–
N25	89.298	134.2	3310	135	51.5	74.5	76.7	82.0	84.3	51.9	66.8	69.2	74.1	76.5	368	290	281	207	207
N26	89.272	135.6	3281	136	58.9	69.8	73.7	75.1	76.1	59.9	62.1	65.9	67.2	68.5	–	–	–	–	–
N27	89.212	136.5	3224	142	55.6	65.6	67.3	69.1	71.5	55.3	57.8	59.5	61.1	63.7	–	–	–	–	–
N28	89.226	136.6	3237	140	58.6	63.7	68.7	71.1	71.8	59.9	56.2	60.8	63.2	64.0	–	–	–	–	–
N29	89.197	137.5	3201	142	31.8	58.3	66.4	68.0	69.7	34.3	51.3	58.5	60.0	61.8	605	511	440	440	439
N30	89.617	295.8	3730	22	42.2	50.1	67.2	72.1	73.3	43.3	51.4	68.0	72.5	73.6	447	443	251	251	251
N31	89.679	298.5	3729	29	31.2	39.6	73.0	76.8	78.3	32.2	40.2	74.1	77.8	79.2	1299	694	302	302	189
N32	89.666	307.4	3732	22	33.8	67.0	76.7	77.7	79.0	35.5	68.1	77.6	78.6	79.9	633	488	286	179	177
N33	89.655	308.0	3732	22	53.9	68.2	76.7	77.4	78.3	55.1	68.9	77.5	78.3	79.2	481	441	437	286	179
N34	89.185	321.9	3598	58	47.7	57.2	61.4	63.7	65.1	50.4	57.3	61.5	63.7	65.1	652	379	379	379	375
N35	89.164	323.0	3581	60	42.7	57.9	63.6	64.8	65.3	44.4	57.0	63.3	64.4	64.9	613	394	379	375	375
N36	89.625	323.6	3728	22	44.9	48.0	63.4	75.4	81.5	45.8	48.6	64.5	76.3	82.5	443	430	403	375	373
N37	89.660	324.1	3730	22	37.0	53.7	81.4	83.6	84.3	38.6	54.9	82.5	84.4	85.1	650	635	283	279	279
N38	89.614	327.2	3726	22	45.7	54.1	61.4	64.4	79.6	46.1	54.2	61.6	64.5	79.8	437	386	288	287	279
N39	89.345	330.9	3659	51	31.2	49.7	51.9	52.8	54.5	32.8	50.0	52.6	53.6	55.3	669	567	567	418	418
N40	89.636	331.0	3728	22	45.6	50.3	66.0	71.0	83.0	45.8	49.7	65.3	70.2	83.8	392	385	300	300	281
N41	89.418	332.5	3685	42	42.4	54.4	56.4	58.2	58.7	44.3	55.7	57.8	59.4	60.0	428	426	422	420	420
N42	89.486	332.7	3706	23	52.5	56.1	56.8	57.8	58.7	54.8	57.3	58.1	59.1	60.1	428	426	426	426	424
N43	89.652	337.4	3728	22	45.3	46.2	50.6	54.0	57.1	45.9	46.0	50.2	53.4	56.5	405	405	405	405	405
N44	89.734	357.5	3733	22	38.3	39.8	41.0	44.1	45.5	39.1	40.0	41.0	43.9	45.0	437	437	437	435	435

Table 4
Persistently illuminated regions near the south pole (see caption for Table 3).

ID #	Location		# Of WAC obs.	Longest temporal gap, hours	Ratio-based illumination percentage					Time-weighted illumination percentage					Longest period in shadow, hours				
	Lat.	Lon.			0.01 km^2	0.25 km^2	1.00 km^2	2.25 km^2	4.00 km^2	0.01 km^2	0.25 km^2	1.00 km^2	2.25 km^2	4.00 km^2	0.01 km^2	0.25 km^2	1.00 km^2	2.25 km^2	4.00 km^2
S01	−89.883	33.5	3999	26	34.8	37.0	38.9	62.7	68.2	35.0	36.8	38.7	62.9	68.6	546	539	539	367	362
S01	−89.918	45.0	3995	26	54.0	64.0	66.0	67.1	68.0	54.7	64.3	66.3	67.4	68.3	381	377	369	369	366
S03	−89.895	47.5	3996	26	57.9	63.9	65.5	67.7	69.7	59.2	64.0	65.8	68.0	70.1	369	369	364	362	356
S04	−89.871	51.2	3997	26	56.5	62.9	66.4	69.6	72.2	57.2	63.0	66.5	69.9	72.5	364	358	356	352	350
S05	−89.806	54.0	3997	26	66.0	77.3	78.2	78.6	78.9	66.8	77.3	78.2	78.5	78.8	241	239	239	239	239
S06	−89.768	57.8	3995	26	57.5	69.6	74.9	76.9	78.2	58.7	69.6	74.8	76.8	78.2	395	339	334	332	239
S07	−89.758	58.4	3995	26	66.6	71.3	73.2	74.9	77.1	67.5	71.2	73.1	74.8	77.1	353	336	332	332	329
S08	−89.682	63.8	3991	25	49.6	54.9	66.9	68.4	69.4	50.5	54.8	66.9	68.4	69.3	342	336	336	330	324
S09	−89.533	78.0	3980	25	44.2	45.8	47.6	49.0	58.2	45.2	46.0	47.7	49.1	57.9	360	356	349	347	347
S10	−89.464	91.6	3972	26	46.3	51.9	52.1	52.5	53.2	46.8	51.5	51.7	52.1	52.8	404	404	404	404	404
S11	−89.446	93.9	3973	26	44.5	49.2	51.7	53.2	53.6	44.8	48.7	51.3	52.8	53.2	411	406	406	404	404
S12	−89.441	95.9	3970	26	45.8	49.7	51.0	52.0	53.9	46.2	49.2	50.6	51.6	53.4	463	459	408	404	404
S13	−89.385	104.4	3963	26	53.1	62.5	64.9	65.3	65.6	52.7	61.8	64.5	64.8	65.2	447	408	403	401	401
S14	−89.366	105.2	3959	26	53.9	62.4	65.0	65.4	65.8	53.9	61.5	64.5	64.9	65.3	448	448	403	403	401
S15	−89.355	111.8	3936	30	52.2	57.4	59.5	60.6	63.2	51.6	56.2	58.6	59.9	62.4	427	424	424	420	417
S16	−89.347	114.3	3926	34	55.0	57.6	59.4	61.6	63.0	54.9	56.4	58.4	60.8	62.3	–	–	–	–	–
S17	−89.333	116.9	3901	39	50.0	59.4	61.1	62.4	64.2	50.2	58.1	60.0	61.3	63.3	–	–	–	–	–
S18	−89.317	120.0	3873	41	53.4	61.6	63.0	64.2	67.9	53.9	59.8	61.4	62.6	66.4	–	–	–	–	–
S19	−89.306	124.0	3833	43	57.7	70.9	71.3	71.3	72.2	58.3	68.2	68.8	69.3	70.3	–	–	–	–	–
S20	−89.299	128.9	3807	83	56.7	67.3	72.1	73.1	74.0	57.0	64.2	69.1	70.2	71.4	–	–	–	–	–
S21	−89.302	132.7	3787	85	53.2	68.0	71.0	71.4	72.3	53.4	64.5	67.6	68.2	69.3	356	337	312	312	312
S22	−89.303	134.2	3783	85	54.0	65.3	68.9	70.2	71.4	53.4	61.8	65.4	66.9	68.3	391	358	337	334	310
S23	−89.463	168.1	3836	51	39.8	60.0	60.8	61.3	61.8	38.6	57.7	58.8	59.4	60.0	466	453	451	451	445
S24	−89.511	173.6	3872	45	53.0	59.9	60.5	60.7	61.4	52.0	58.4	59.2	59.6	60.4	475	467	458	456	454
S25	−89.595	184.0	3928	36	55.9	61.2	66.0	68.3	70.2	55.9	60.4	65.2	67.5	69.4	355	353	350	350	214
S26	−89.606	187.0	3931	34	59.2	67.8	69.1	70.0	70.3	58.4	66.9	68.2	69.2	69.6	–	–	–	–	–
S27	−89.649	191.1	3957	26	55.2	64.5	67.5	70.9	76.9	55.2	63.8	66.6	70.0	76.0	372	370	370	143	142
S28	−89.685	196.7	3965	26	69.0	87.4	88.4	88.7	89.2	68.4	86.3	87.2	87.5	88.1	147	70	66	64	60
S29	−89.667	197.0	3961	26	63.1	68.5	87.4	87.9	88.5	62.9	67.3	86.2	86.8	87.4	378	227	72	70	66
S30	−89.740	201.2	3969	26	71.6	80.2	83.7	86.1	87.9	71.7	79.4	82.8	85.2	87.0	145	75	72	66	62
S31	−89.791	204.7	3973	26	65.8	80.7	88.6	89.1	89.8	66.3	79.6	87.8	88.3	89.0	170	130	64	62	58
S32	−89.802	205.1	3973	26	67.6	79.8	82.4	89.0	89.5	67.9	78.9	81.5	88.3	88.8	141	128	126	62	62
S33	−89.808	205.9	3974	26	63.0	79.9	80.6	83.5	89.5	63.4	79.0	79.7	82.6	88.8	155	126	126	126	62
S34	−89.366	208.1	3841	64	51.4	57.8	59.1	59.3	60.4	50.5	55.4	56.7	57.0	58.1	407	407	396	396	379
S35	−89.844	208.5	3980	26	65.4	76.3	78.3	79.4	80.6	65.9	75.8	77.6	78.8	80.0	189	149	147	141	140
S36	−89.859	208.7	3984	26	62.1	75.4	77.6	78.6	79.7	62.9	75.0	77.1	78.0	79.1	239	183	149	149	141
S37	−89.237	212.3	3774	77	53.1	55.3	56.4	57.5	58.0	52.8	51.7	52.9	54.1	54.6	381	353	345	343	343
S38	−89.900	212.9	3986	26	58.5	73.1	74.6	75.8	77.0	59.6	72.9	74.4	75.6	76.8	239	235	185	185	183
S39	−89.290	214.0	3818	70	49.9	58.4	60.5	61.9	62.9	49.0	55.3	57.4	58.8	59.9	372	343	339	339	338
S40	−89.962	214.4	3990	26	60.2	65.7	67.9	69.9	72.3	60.9	65.7	68.0	70.0	72.5	254	254	241	241	239
S41	−89.564	214.8	3949	26	53.4	69.7	71.4	72.9	75.1	53.7	69.1	70.9	72.3	74.5	233	179	177	177	170
S42	−89.336	216.7	3851	62	55.1	60.7	64.1	65.9	67.2	53.9	58.2	61.4	63.3	64.7	400	347	334	332	332
S43	−89.502	218.3	3930	28	53.9	59.6	61.7	82.7	85.7	53.9	58.9	61.1	81.4	84.3	321	310	310	109	104
S44	−89.419	219.2	3901	41	61.4	63.9	69.5	74.1	83.4	60.4	62.0	67.4	72.0	81.0	314	312	268	259	168
S45	−89.332	219.4	3860	60	54.7	55.0	59.1	62.5	67.3	54.0	52.6	56.7	60.0	65.2	367	367	334	332	332
S46	−89.418	221.3	3907	40	64.2	68.5	76.2	89.3	92.5	63.3	66.3	73.8	86.9	90.5	308	294	197	141	89
S47	−89.503	221.8	3944	26	55.1	67.6	82.8	87.5	88.9	56.1	66.6	80.9	86.1	87.5	281	238	96	92	83
S48	−89.361	226.5	3907	38	56.3	64.5	66.3	67.3	68.5	56.8	62.9	64.8	65.9	67.1	346	264	259	259	259
S49	−89.346	227.7	3909	38	55.6	60.1	65.1	66.0	67.4	56.3	58.6	63.7	64.6	66.1	273	269	269	266	259
S50	−89.904	227.8	3989	26	34.7	37.7	65.9	73.9	75.0	35.2	37.3	65.7	73.9	75.0	519	505	234	234	222
S51	−89.992	258.7	3991	26	61.8	64.4	66.3	67.8	69.3	62.8	64.6	66.7	68.2	69.7	356	356	356	356	241

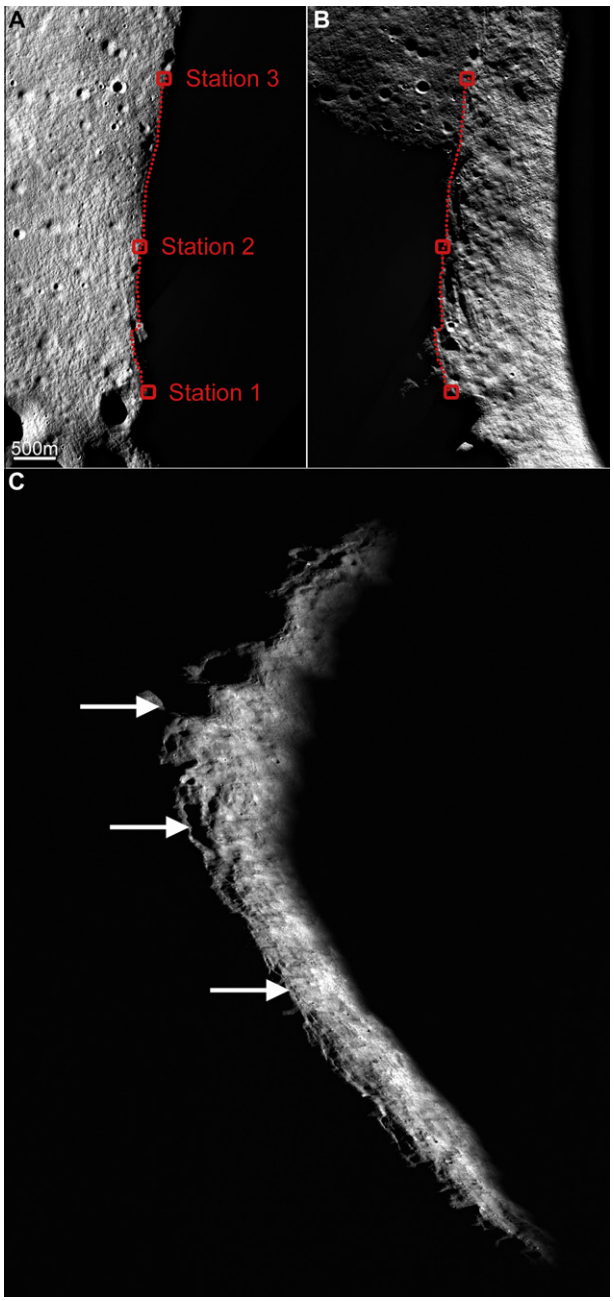

Fig. 15. Station 1 (89.685°S, 196.7°E), Station 2 (89.740°S, 201.2°E), and Station 3 (89.808°S, 205.9°E) are collectively illuminated for 92.1% of the year with the longest eclipse period lasting only 43 h. Each box represents a 0.01 km^2 region; single WAC pixel. (A) is a NAC mosaic of M114880090L/R, M114859732L/R with the subsolar longitude of ~290°E. (B) is a NAC mosaic of M139695762R, M139709342R, M139722912R, M139729686R, M139743255R, and M139756842R with the subsolar longitude of ~20°E. The dotted lines in (A) and (B) denote potential traverse options. (C) Oblique view (M185374654L/R) of the rim of Shackleton crater acquired during the winter solstice (subsolar point: 1.55°N, 61.5°E). The arrows mark the locations of the three stations (Station 1 is at the top of the image and Station 3 is at the bottom).

least energy traverses and identify optimal locations for stationary assets. Comparatively, Bussey et al. (2010) identified a point on the rim of Shackleton crater, and a point on a ridge 10 km away in the 474 m/pixel Kaguya DEM, that collectively remained illuminated for a similar portion of the year (~94%). However, the two points in that study (Bussey et al., 2010) were simultaneously eclipsed for 60 h during the winter and were further apart than the three stations identified above.

In addition to the rim of Shackleton crater, there are many opportunities for a mobile polar robotic/human explorer to investigate other nearby sites of interest. Heading away from the south pole along the 205°E meridian is a flat region that also harbors several local topographic highs that receive extended illumination over the lunar year, including a 0.01 km^2 region located at 89.418°S, 221.3°E and 89.500°S, 222.1°E, which were illuminated for 63.3% and 45.6% of the lunar year respectively. This region was coarsely identified in Clementine images and later refined both spatially and temporally with numerical models (Nozette et al., 1996; Bussey et al., 1999, 2010; Garrick-Bethell et al., 2005; Noda et al., 2008; Bryant, 2009, Mazarico et al., 2010). By traversing between or configuring solar panel arrays at these two locations, which are 2.5 km apart, assets could remain illuminated for 91.8% of the lunar year with the longest period of shadow lasting 107 h. Additional mobility around each site (~100 m) increases the illuminated period to 94.2% of the year with the longest eclipsed period lasting 78 h and greatest period of uninterrupted illumination between these sites lasting 5592 h (66% of the lunar year).

Study of LROC NAC images also revealed numerous, small permanently shadowed regions adjacent to these persistently illuminated highs. Large permanently shadowed regions generally have long, steep slopes and, by definition, no easy access to direct solar energy making it difficult to traverse and survive for long periods of time. Conversely, small shadowed features found in these small persistently illuminated regions are easily accessible and a several meter mast (Bryant, 2009; Mazarico et al., 2010) could collect solar energy to support operations while the base of the explorer is in permanent shadow. Furthermore, a polar rover could explore a series of these small permanently shadowed regions with standoff instrumentation that would require substantially less power than needed to explore the larger and less accessible permanently shadowed regions (i.e. Shackleton crater).

5.2. Peary crater

Lucchitta (1978) identified Peary crater as being pre-Nectarian in age. A bulk of the floor of Peary is filled with plains material, most likely emplaced during the impact that created Imbrium basin. The outside of the crater is composed of degraded ridges, hills, depressions that are Nectarian and pre-Nectarian in age. This topography limits the duration a single 0.01 km^2 point on the surface remains illuminated to less than 64% of the lunar year (Figs. 5B and 7B and Tables 2 and 3). Furthermore, the WAC image data did not reveal any 0.01 km^2 regions with fewer than 298 h of persistent shadow, creating less benign thermal conditions than found at the south pole. However, just as in the case of the south polar region, surface mobility or a distributed array of solar panels extended the amount of time illuminated and reduced the time in shadow.

There are three locations that offer relatively persistent illumination on topographic highs on the northern rim of Peary crater. The regions were first recognized in Clementine images collected during northern summer, which showed the three regions illuminated in all 53 UVVIS images studied (Nozette et al., 1996; Bussey et al., 2005). However, later DEM based simulations showed that these potential permanently illuminated regions were eclipsed by the horizon for significant periods of time in the winter (Garrick-Bethell et al., 2005; Noda et al., 2008; Bryant, 2009, Mazarico et al., 2010). The first region (89.366°N, 128.0°E) to consider is on the rim of Whipple crater, which is superimposed on the rim of Peary crater. This 2.0 km × 2.0 km (4.0 km^2) region remained illuminated in 85.9% of the WAC observations acquired with the longest period of persistent shadow lasting 207 h. The second region (89.816°N, 117.3°E) lies on the rim of Peary halfway

between Whipple and Hinshelwood craters. This 2.0 km × 2.0 km (4.0 km^2) region was illuminated for 80.7% of the year, with its longest period of eclipse lasting 142 h. Near Hinshelwood crater, which is also superimposed on the rim of Peary crater, are two 0.01 km^2 regions located 1.5 km apart (89.636°N, 331.0°E and 89.660°N, 324.1°E) that were collectively illuminated 80.1% of the lunar year studied with the longest eclipsed period lasting 284 h. These regions offer unique areas to explore, however engineering constraints based on the percentage of time the surface is illuminated and the longest period of time in shadow may limit exploration to one or possibly all three of these regions.

6. Conclusions

The Moon's slightly tilted axis results in regions near the poles to remain permanently shadowed while other nearby areas have extended periods of illumination. Lighting conditions of the poles were previously studied with Clementine UVVIS data and topographic models from Earth based radar and laser altimeters mounted on orbiting spacecraft. LROC complements these analyses with higher resolution data (up to meter scale) that delimit and allow the quantification of lighting conditions near both lunar poles, which enable more precise landing site selections and traverse analyses for both human and robotic polar missions.

Similar to previous studies that characterized the illumination environment over a full lunar year (Noda et al., 2008; Bussey et al., 2010; Mazarico et al., 2010), the LROC dataset has not revealed any truly permanently illuminated locations. Although there are several topographic highs near the lunar pole that are ideal candidates for permanent illumination, analysis of WAC multi-temporal movie sequences and high resolution NAC images show that crater rims, mountain ranges, and other massifs located around these features prohibit year-round lighting on a topographic facet or even around the circumference of a summit. Furthermore, during lunar eclipses, where the Moon traverses through the Earth's umbra, the entire polar region goes dark for some period of time. Therefore, there are no regions on the Moon that are *permanently* illuminated; however, a series of closely located sites, such as topographic highs along the rim of Shackleton crater, do exist and collectively provide solar illumination with the longest period in shadow lasting *only 43* h. Together, these stations received sunlight for 93.7% of a year and remained continuously illuminated for 4960 h (over 58% of the lunar year). With these persistently illuminated sites near both poles, mobile and stationary assets benefit from near-continuous access to solar energy and benign thermal conditions (Heiken et al., 1991). These persistently illuminated regions are also adjacent to large permanently shadowed areas (e.g. the floor of Shackleton crater) that are of interest to both scientists and engineers prospecting for cold-trapped volatiles for in situ resource utilization. Additionally, there are many small permanently shadowed features that are shallow enough to be explored while receiving solar energy with a panel attached to a small boom.

Together the multi-temporal and high resolution views provided by the LROC WAC and NAC provide the means to accurately characterize lighting conditions at a scale of 100 m, while also providing meter scale maps for planning future human and robotic missions to these key sites. In December of 2011, LRO transitioned into a frozen orbit, which provides broader coverage near the north pole with lower resolution (ground sampling distance of 2 m for the NAC, and 300 m for the WAC) while providing opportunities for higher resolution imaging (ground sampling distance of 0.6 m for the NAC, and 60 m for the WAC) with smaller observation footprints in the south polar region. Continued imaging throughout the lifetime of the mission will enable better characterization of the lighting environment near these persistently illuminated sites, thus providing a key dataset for future science and exploration missions to polar regions.

Acknowledgments

The authors wish to thank Kris Becker and Jeff Anderson at the USGS for providing technical expertise and implementing refinements to the geometric camera models for the WAC and NAC. We also acknowledge Erwan Mazarico and Gregory Neumann of the LOLA team for providing accurate and precise ephemeris that enabled our detailed and quantitative illumination maps. Finally, we would like to recognize both of our anonymous reviewers who provided great recommendations that greatly enhanced this work.

The raw, calibrated, and map projected image data reported in this paper are archived with the Planetary Data System Imaging Node (http://lroc.sese.asu.edu/data/).

Appendix A. Supplementary material

Supplementary data associated with this article can be found, in the online version, at http://dx.doi.org/10.1016/j.icarus.2012.10.010.

References

Bryant, S., 2009. Lunar pole illumination and communications maps computed from Goldstone Solar System Radar elevation data. In: Proc. IEEE Aerospace Conf. http://dx.doi.org/10.1109/AERO.2009.4839375.

Burke, J.D., 1985. Merits of a lunar polar base location. In: Mendell, W.W. (Ed.), Lunar Bases and Space Activities of the 21st Century. Lunar and Planetary Institute, Houston, TX, pp. 77–84.

Bussey, D.B.J., Spudis, P.D., Robinson, M.S., 1999. Illumination conditions at the lunar south pole. Geophys. Res. Lett. 9, 1187–1190.

Bussey, D.B.J., Fristad, K.E., Shenk, P.M., Robinson, M.S., Spudis, P.D., 2005. Constant illumination at the lunar north pole. Nature 434, 842. http://dx.doi.org/10.1038/434842a.

Bussey, D.B.J., McGovern, J.A., Spudis, P.D., Neish, C.D., Noda, H., Ishihara, Y., Sørensen, S.-A., 2010. Illumination conditions of the south pole of the Moon derived using Kaguya topography. Icarus 207, 558–564. http://dx.doi.org/10.1016/j.icarus.2010.03.028.

Bussey, D.B.J., and the Mini-RF Team, 2011. Mini-RF: Mapping the Moon with Radar. EGU General Assembly, EGU2011-11798.

Campbell, B.A., Campbell, D.B., Chandler, J.F., Hine, A.A., Nolan, M.C., Perillat, P.J., 2003. Radar imaging of the lunar poles. Nature 426, 137–138. http://dx.doi.org/10.1038/426137a.

Colaprete, A. et al., 2010. Detection of water within the LCROSS ejecta plume. Science 330, 463–468. http://dx.doi.org/10.1126/science.1186986.

Feldman, W. et al., 2000. Polar hydrogen deposits on the Moon. J. Geophys. Res. 105, 4175–4195. http://dx.doi.org/10.1029/1999JE001129.

Garrick-Bethell, I., Byrne, S., Hoffman, J.A., Zuber, M.T., 2005. Areas of favorable illumination at the lunar poles calculated from topography. Lunar Planet. Sci. Abstract #2006.

Goddard, E.C., Pendray, G.E. (Eds.), 1970. The Papers of Robert H. Goddard. McGraw-Hill, New York, NY.

Gonzalez, R.C., Woods, R.E., 1992. Digital Image Processing, third ed. Addison-Wesley Publishing, Reading, Massachusetts.

Heiken, G., Vaniman, D., French, B.M., 1991. Lunar Sourcebook: A User's Guide to the Moon. Cambridge University Press, Cambridge, England; New York..

Hurley, D.M., Lawrence, D.J., Bussey, D.B.J., Vondrak, R.R., Elphic, R.C., Gladstone, G.R., 2012. Two-dimensional distribution of volatiles in the lunar regolith from space weathering simulations. Geophys. Res. Lett. 39, L09203. http://dx.doi.org/10.1029/2012GL051105.

Ingersoll, A.P., Svitek, T., Murray, B.C., 1992. Stability of polar frosts in spherical bowl-shaped craters on the Moon, Mercury, and Mars. Icarus 100, 40–47. http://dx.doi.org/10.1016/0019-1035(92)90016-Z.

Laskar, J., Joutel, F., Robutel, P., 1993. Stabilization of the Earth's obliquity by the Moon. Nature 361, 615–617. http://dx.doi.org/10.1038/361615a0.

Lucchitta, B.K., 1978. Geologic Map of the North Side of the Moon. U.S. Geol. Surv., Map, I-1062.

Margot, J.L., Campbell, D.B., Jurgens, R.F., Slade, M.A., 1999. Topography of the lunar poles from radar interferometry: A survey of cold trap locations. Science 284, 1658–1660. http://dx.doi.org/10.1126/science.284.5420.1658.

Mazarico, E., Neumann, G.A., Smith, D.E., Zuber, M.T., Torrence, M.H., 2010. Illumination conditions of the lunar polar regions using LOLA topography. Icarus 211, 1066–1081. http://dx.doi.org/10.1016/j.icarus.2010.10.030.

Mazarico, E. et al., 2011. Orbit determination of the Lunar Reconnaissance Orbiter. J. Geodesy, in press. http://dx.doi.org/10.1007/s00190-011-0509-4.
McEwen, A.S., Robinson, M.S., 1997. Mapping of the Moon by Clementine. Adv. Space Res. 19 (10), 1523–1533. http://dx.doi.org/10.1016/S0273-1177(97)00365-7.
Mitrofanov, I.G. et al., 2010. Hydrogen mapping of the lunar south pole using the LRO Neutron Detector Experiment LEND. Science 330, 483–486. http://dx.doi.org/10.1126/science.1185696.
Mutch, T.A., 1970. Geology of the Moon: A Stratigraphic View. Princeton Univ. Press, Princeton, NJ.
Noda, H. et al., 2008. Illumination conditions at the lunar polar regions by Kaguya (SELENE) laser altimeter. Geophys. Res. Lett. 35, L24203. http://dx.doi.org/10.1029/2008GL035692.
Nozette, S. et al., 1994. The Clementine mission to the Moon: Scientific overview. Science 266, 1835–1839. http://dx.doi.org/10.1126/science.266.5192.1835.
Nozette, S. et al., 1996. The Clementine bistatic radar experiment. Science 274, 1495–1498. http://dx.doi.org/10.1126/science.274.5292.1495.
Nozette, S. et al., 2010. The Lunar Reconnaissance Orbiter Miniature Radio Frequency (Mini-RF) technology demonstration. Space Sci. Rev. 150, 285–302. http://dx.doi.org/10.1007/s11214-009-9607-5.
Nozette, S., Spudis, P.D., Robinson, M.S., Bussey, D.B.J., Lichtenberg, C., Bonner, R., 2001. Integration of lunar polar remote-sensing data sets: Evidence for ice at the lunar south pole. J. Geophys. Res. 106, 23253–23266. http://dx.doi.org/10.1029/2000JE001417.
Paige, D.A. et al., 2010. Diviner lunar radiometer observations of cold traps in the Moon's south polar region. Science 330, 479–482. http://dx.doi.org/10.1126/science.1187726.
Robinson, M.S. et al., 2010. Lunar Reconnaissance Orbiter Camera (LROC) instrument overview. Space Sci. Rev. 150, 81–124. http://dx.doi.org/10.1007/s11214-010-9634-2.
Shoemaker, E.M., Robinson, M.S., Eliason, E., 1994. The south pole region of the Moon as seen by Clementine. Science 266, 1851–1854.
Shevchenko, V.V., 1999. Lunar base siting. In: Eckart, P. (Ed.), The Lunar Base Handbook: An Introduction to Lunar Base Design, Development, and Operations. McGraw-Hill, New York, NY, pp. 205–222.
Siegler, M.A., Bills, B.G., Paige, D.A., 2011. Effects of orbital evolution on lunar ice stability. J. Geophys. Res. 116, E03010. http://dx.doi.org/10.1029/2010JE003652.
Smith, D.E. et al., 2010. Initial observations from the Lunar Orbiter Laser Altimeter. Geophys. Res. Lett. 37, L18204. http://dx.doi.org/10.1029/2010GL043751.
Speyerer, E.J. et al., 2012. In-flight geometric calibration of the Lunar Reconnaissance Orbiter Camera. In: The XXII Congress of the International Society of Photogrammetry and Remote Sensing.
Spudis, P.D. et al., 2010. Initial results for the north pole of the Moon from Mini-SAR, Chandrayaan-1 mission. Geophys. Res. Lett. 37, L06204. http://dx.doi.org/10.1029/2009GL042259.
Spudis, P.D., Bussey, D.B.J., Plescia, J., Josset, J.-L., Beauvivre, S., 2008. Geology of Shackleton crater and the south pole of the Moon. Geophys. Res. Lett. 35, L14201. http://dx.doi.org/10.1029/2008GL034468.
Tooley, C.R. et al., 2010. Lunar Reconnaissance Orbiter mission and spacecraft design. Space Sci. Rev. 150, 23–62. http://dx.doi.org/10.1007/s11214-009-9624-4.
Urey, H.C., 1952. The Planets: Their Origin and Development. Yale University Press, New Haven, CT.
Ward, W.R., 1975. Past orientation of the lunar spin axis. Science 189, 377–379. http://dx.doi.org/10.1126/science.189.4200.377.
Watson, K., Murray, B.C., Brown, H., 1961. The behavior of volatiles on the lunar surface. J. Geophys. Res. 66, 3033–3045.
Wilhelms, D.E., Howard, K.A., Wilshire, H.G., 1979, Geologic Map of The South Side of The Moon. U.S. Geol. Surv., Map, I-1162.
Zuber, M. et al., 2012. Constraints on the volatile distribution within Shackleton crater at the lunar south pole. Nature 486, 378–381. http://dx.doi.org/10.1038/nature11216.